JOURNAL OF GEOPHYSICAL RESEARCH, VOL. 115, B05402, doi:10.1029/2009JB006612, 2010

Inferring mantle properties with an evolving dynamic model of the Antarctica-New Zealand region from the Late Cretaceous

Sonja Spasojevic,[1] Michael Gurnis,[1] and Rupert Sutherland[2]

Received 12 May 2009; revised 3 December 2009; accepted 18 December 2009; published 14 May 2010.

[1] We show that time-dependent models of mantle upwellings above a cold downwelling in the New Zealand-Antarctica region since 80 Ma can explain anomalous geophysical observations: ~1.0 km of positive residual bathymetry at the Antarctica margin, a large Ross Sea geoid low, 0.5–0.9 km of excess tectonic subsidence of the Campbell Plateau since 80 Ma, and several seismic wave speed anomalies. Model results indicate that the largest mantle upwelling, centered in the Ross Sea, has an average temperature anomaly of 200°C and density anomaly of 0.6%, and it rose from midmantle depths at 80 Ma to a present depth of 400–1000 km. Anomalous Campbell Plateau subsidence requires a smaller hot anomaly evolving within the upper mantle under the region of the reconstructed Late Cretaceous Campbell Plateau. The excess subsidence of the plateau results from northward drift of New Zealand away from the dynamic topography high created by the smaller hot anomaly. To fit present-day geoid and residual topography observations, we require a large lower:upper mantle viscosity ratio of 100:1. We suggest that the distribution of temperature and viscosity is related to long-lived Gondwana subduction that accumulated high-density, high-viscosity lower mantle below a chemically altered upper mantle with anomalously low density and/or high temperature. Time-dependent observations enable constraints on absolute viscosities of 10^{23} Pa s and 10^{21} Pa s for the lower and upper mantle, respectively.

Citation: Spasojevic, S., M. Gurnis, and R. Sutherland (2010), Inferring mantle properties with an evolving dynamic model of the Antarctica-New Zealand region from the Late Cretaceous, *J. Geophys. Res.*, *115*, B05402, doi:10.1029/2009JB006612.

1. Introduction

[2] Conjugate passive continental margins of Antarctica (ANT) and New Zealand (NZ) lie at the edges of Marie Byrd Land and the Campbell Plateau, respectively. The ANT margin and adjacent ocean crust has approximately 1 km of positive residual bathymetry, relative to both the NZ margin and a reference age-depth model for the Pacific Ocean [*Sutherland et al.*, 2010]. This ANT bathymetric anomaly is spatially correlated with a geoid minimum in the Ross Sea [*Förste et al.*, 2008]. Seismic tomography reveals low velocities within and beneath the lithosphere, low velocities in the transition zone and uppermost lower mantle, and high velocities in the lowermost mantle [e.g., *Grand*, 2002; *Gu et al.*, 2001; *Masters et al.*, 2000; *Ritsema and van Heijst*, 2000]. Campbell Plateau (NZ) boreholes record excess tectonic subsidence of 500–900 m, with a maximum in tectonic subsidence rate at 70–40 Ma, coincident with rapid northward drift of NZ away from ANT [*Cook et al.*, 1999; *Sutherland et al.*, 2010]. Mantle upwelling beneath the ANT margin has been suggested on the basis of these anomalous observations [*Sieminski et al.*, 2003; *Sutherland et al.*, 2010], and is consistent with previous suggestions based on the distribution and chemistry of igneous rocks [*Storey et al.*, 1999; *Weaver et al.*, 1994].

[3] In a previous paper [*Sutherland et al.*, 2010], we presented observations of anomalous topography and subsidence, showed that a simplified geodynamic model of mantle upwelling could be constructed to fit all observations, and we proposed a hypothesis that such an upwelling may have followed the Cretaceous termination of long-lived subduction (>200 Myr) at the Gondwana margin. In this paper, we document and analyze a range of geodynamic models for the evolving mantle flow, and hence we are able to draw conclusions about mantle properties. Our models incorporate mantle upwellings and a downwelling that are geometrically simplified, and are required to evolve to features equivalent to the three anomalous velocity structures imaged in global seismic-tomographic inversions, and we must fit observations of geoid, topography, and subsidence history from 80 Ma to the present.

[4] First, we utilize global time-dependent geodynamic models to constrain the magnitude of buoyancy anomalies and their initial Late Cretaceous geometry and depth. Second, we fit time-dependent (tectonic subsidence) and present-day (geoid, seismic tomography and residual bathymetry) observations jointly, to constrain both the relative and absolute values of mantle viscosities in the ANT-NZ region.

[1]Seismological Laboratory, California Institute of Technology, Pasadena, California, USA.
[2]GNS Science, Lower Hutt, New Zealand.

0148-0227/10/2009JB006612

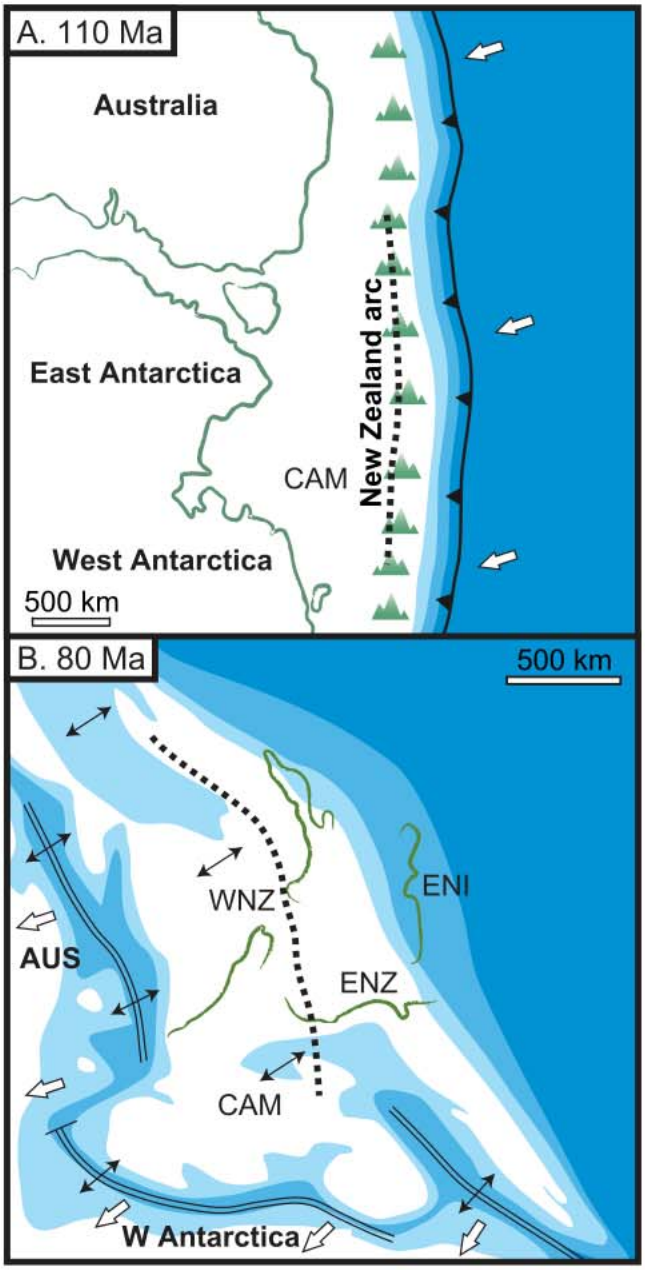

Figure 1. Cartoons showing the configuration of Australia, Antarctica, New Zealand and the Campbell Plateau (CAM) at a time (a) when Gondwana had an active subduction zone and arc and (b) when incipient development of the Tasman Sea and South Pacific Ocean during widespread rifting led to final Gondwana breakup. The modern coastline of fragments of western New Zealand (WNZ), eastern South Island (ENZ), and eastern North Island (ENI) are shown, with Cenozoic relative motions reconstructed [*Sutherland,* 1995; *King,* 2000]. The position of the reconstructed Gondwana arc in the New Zealand region is shown dotted [*Sutherland*, 1999a, 1999b]. Shades show land (white), shelf (light shade, <400 m), slope (medium shade, 400–3000 m), and abyssal (dark shade, >3000 m) paleodepths. Open arrows show plate motion directions relative to New Zealand, and double-ended arrows show extension directions during rifting.

Geoid observations provide a strong constraint on the radial viscosity gradient in the mantle, and we show that absolute viscosity can also be constrained when seismic tomography is combined with constraints on present-day and evolving dynamic topography. Third, we investigate the association of the observed ANT geoid low with mantle upwelling, which makes this region of particular geodynamic interest, because upwellings are more usually associated with geoid highs [*Richards et al.*, 1988].

2. Tectonic History

[5] The ANT-NZ region today has conjugate passive margins that are separated by seafloor spreading at the Pacific-Antarctic Rise [*Cande et al.*, 1995; *Molnar et al.*, 1975], but it was previously a region characterized by a long-lived subduction zone that was active over much of the Late Paleozoic and Mesozoic [*Adams et al.*, 2007; *Mortimer et al.*, 1999; *Veevers*, 2000]. Mesozoic activity along the eastern Gondwana subduction zone (Figure 1) occurred from offshore eastern Australia, New Caledonia, and the Lord Howe Rise [*Adams et al.*, 2007; *Mortimer et al.*, 1998; *Paris*, 1981; *Veevers et al.*, 1994], through New Zealand and the Chatham Rise [*Bradshaw*, 1989; *Davy et al.*, 2008; *Kimbrough et al.*, 1994; *Mortimer et al.*, 1999], to Marie Byrd Land in Antarctica [*Bradshaw et al.*, 1997; *Mukasa and Dalziel*, 2000; *Weaver et al.*, 1994]. Subduction continued during the Cenozoic in the Thurston Island and Antarctic Peninsula regions [*Cunningham et al.*, 2002; *Dalziel and Elliot*, 1982; *Larter et al.*, 2002; *Storey and Nell*, 1988], and the subduction zone is still active today in western South America [*Allmendinger et al.*, 1997; *Herve et al.*, 2007].

[6] The termination of subduction was earliest in the New Zealand sector, where the youngest subduction-related igneous rocks formed at ~115–105 Ma [*Kimbrough et al.*, 1994; *Mortimer et al.*, 1999; *Muir et al.*, 1995, 1998; *Waight et al.*, 1998], and this time corresponds to the end of local convergent deformation [*Mazengarb and Harris*, 1994] and the onset of widespread rifting and intraplate (anorogenic, A-type) magmatism [*Laird and Bradshaw*, 2004; *Weaver et al.*, 1994]. Subduction termination was slightly later at ~105–95 Ma in Marie Byrd Land [*Bradshaw et al.*, 1997; *Mukasa and Dalziel*, 2000; *Storey et al.*, 1999], and was not until Cenozoic time (<65 Ma) in the Thurston Island and Antarctic Peninsula regions [*Cunningham et al.*, 2002; *Larter et al.*, 2002; *McCarron and Larter*, 1998; *Storey and Nell*, 1988].

[7] Gondwana breakup and voluminous magmatism, which is interpreted to have been plume-related [*Pankhurst et al.*, 2000; *Storey*, 1995], commenced during the Jurassic at ~180 Ma as South America, Africa and the Weddell Sea region of Antarctica started to separate and form the South Atlantic and Southern Ocean [*Ferris et al.*, 2000; *Pankhurst et al.*, 2000; *Storey*, 1995]. By ~120 Ma (Early Cretaceous; Aptian), Gondwana was fragmented everywhere but the New Zealand sector, and the fragments were starting to disperse as seafloor spreading ridges were established [*Lawver et al.*, 1987; *Marks and Tikku*, 2001; *Müller et al.*, 2000; *Nürnberg and Müller*, 1991]. The final stage of Gondwana breakup (Figure 1) created the Marie Byrd Land and Campbell Plateau passive margins at ~83–79 Ma as

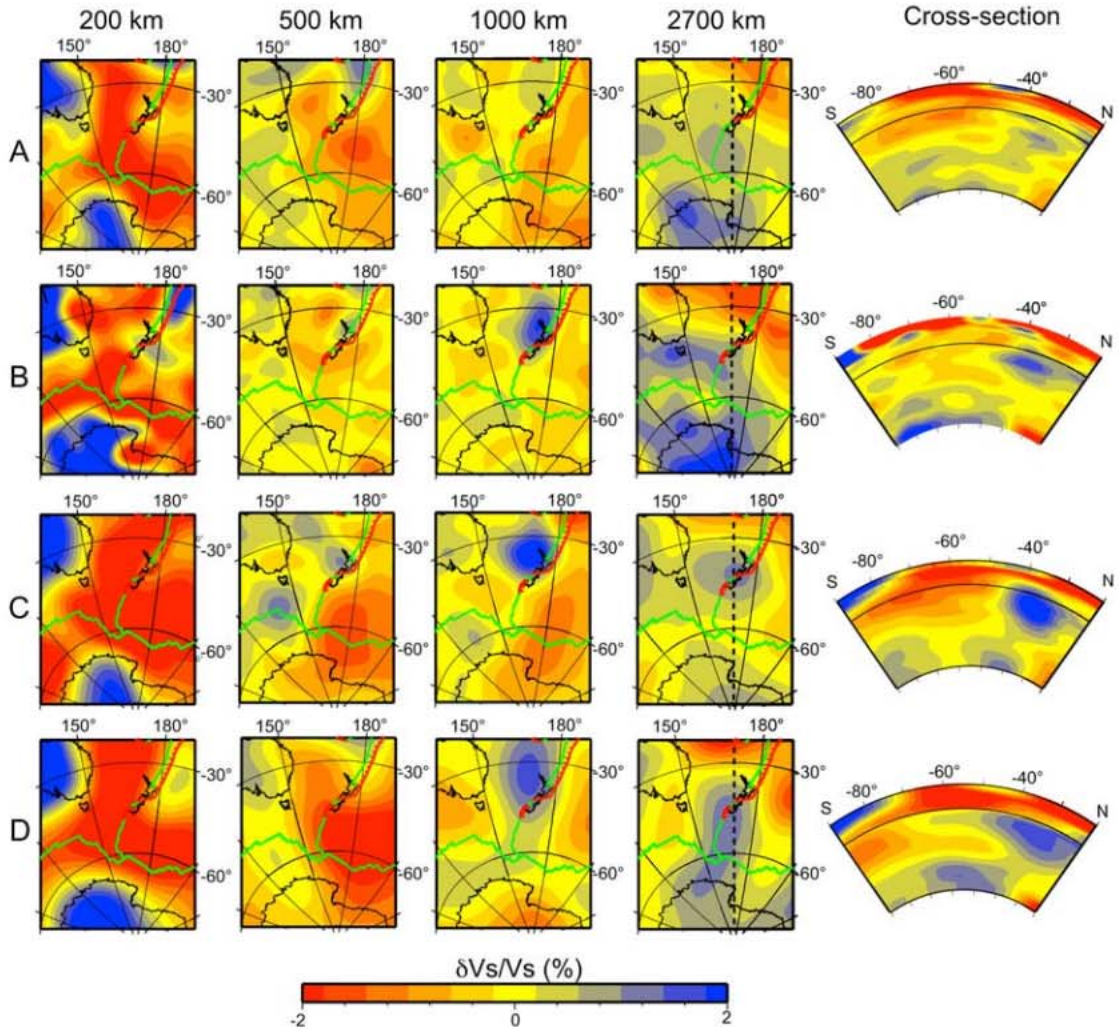

Figure 2. Shear wave seismic tomography maps in the Antarctica-New Zealand region at 200, 500, 1000, and 2700 km depths and N-S cross section along 170°E from (a) *Ritsema and van Heijst* [2000], (b) *Grand* [2002], (c) *Masters et al.* [2000], and (d) *Gu et al.* [2001]. The position of cross section is shown on depth slices at 2700 km. The lateral resolution of models varies between 275 km [*Grand*, 2002] and ~1000 km [*Ritsema and van Heijst*, 2000].

New Zealand, Australia and Antarctica separated to form the Tasman Sea and South Pacific sector of the Southern Ocean [*Cande et al.*, 1995; *Gaina et al.*, 1998; *Molnar et al.*, 1975; *Stock and Molnar*, 1987; *Sutherland*, 1999a; *Weissel et al.*, 1977].

3. Observational Constraints

[8] Global [*Grand*, 2002; *Gu et al.*, 2001; *Masters et al.*, 2000; *Ritsema and van Heijst*, 2000] and regional [*Ritzwoller et al.*, 2001; *Sieminski et al.*, 2003] seismic tomographic inversions appear to resolve three anomalous structures in the NZ-ANT region (Figure 2): A broad lithospheric and sublithospheric low-velocity anomaly; a low-velocity anomaly spanning the transition zone and upper part of the lower mantle; and a high-velocity anomaly in the lowermost mantle. The lithospheric and sublithospheric mantle of West Antarctica (including the Ross Sea and Marie Byrd Land) is characterized by a broad anomaly of low seismic velocities at <400 km depth (Figure 2). The intermediate-depth low-velocity anomaly spans the transition zone and upper part of the lower mantle between ~400 and 1100 km depths (Figure 2). Finally, a region of high *S* wave velocities above the core-mantle boundary (CMB) has a depth extent of approximately 2000–2900 km (Figure 2), and is attributed to high-density material that accumulated during Paleozoic and Mesozoic Gondwana subduction.

[9] The details of three anomalous structures differ between tomographic models (Figure 2). The shallowest low-velocity anomaly appears to be connected to a much larger shallow low-seismic-velocity anomaly that is spatially correlated with the location of Late Cretaceous and Cenozoic seafloor spreading and continental extension for all of the tomographic inversions (Figure 2). Only one model (Figure 2b; *Grand* [2002]) has a localized circular low-velocity lithospheric-sublithospheric anomaly in the Ross Sea region.

[10] The intermediate-depth low-velocity anomaly seems to be spatially more localized than the shallow anomaly and all of the inversions resolve it to the east from the Macquarie Ridge (Figure 2), plate boundary between the Pacific and Australian plates extending south of South Island, New Zealand. At 1000 km depth, based on models by *Masters et al.* [2000] (Figure 2a) and *Ritsema and van Heijst* [2000] (Figure 2c), this anomaly appears to span between ANT and NZ across the Antarctic-Pacific ridge, while the model by *Gu et al.* [2001] defines two separate anomalies (Figure 2d). A low-velocity anomaly in this depth range has previously been interpreted as a mantle upwelling on the basis of regional tomographic inversions [*Sieminski et al.*, 2003]. In addition, in the Ross Sea region the mantle transition zone is inferred from SS and PP precursors to be >20 km thinner than the global average at long wavelengths [*Flanagan and Shearer*, 1998; *Houser et al.*, 2008]. Such a thinning is consistent with a vertically coherent warm (>150°C; seismically low velocity) anomaly that spans 410–650 km depths [*Bina and Helffrich*, 1994; *Houser et al.*, 2008]; this suggests that a part of the intermediate-depth low-velocity anomaly could be associated with mantle upwelling.

[11] Details of the high-velocity anomaly in the lower mantle differ significantly between models (Figure 2), with all models defining it in the region of interest between the Ross Sea and Marie Byrd Land. Several models (Figures 2a, 2b, and 2d) connect the ANT lower-mantle anomaly with high-velocity anomalies located further north and northwest, consistent with the hypothesis that the anomaly corresponds to slabs created during long-lived Mesozoic subduction [*Chase and Sprowl*, 1983; *Gurnis et al.*, 1998]. All models have this anomaly restricted to the lower portion of the lower mantle (Figure 2).

[12] One of the largest geoid minimums, with an amplitude of about −60 m over a wavelength of several thousand kilometers [*Förste et al.*, 2008], is centered in the Ross Sea (Figure 3a), roughly coincident with the midmantle seismic-velocity low (Figure 2) and transition-zone thickness anomaly [*Houser et al.*, 2008]. *Chase and Sprowl* [1983] suggest that the global semicontinuous geoid low, passing from Hudson's Bay through Siberia and India to Antarctica and the Ross Sea (Figure 3a), is correlated with the position of long-lived Mesozoic subduction. On the other hand, the large-scale residual geoid highs, obtained after subtracting the putative effects of subduction, are correlated with locations of present-day hot spots [*Chase*, 1985]. There is a positive correlation between geoid highs and low seismic velocity in the lower mantle at degree 2, and with low seismic velocity in the upper mantle at degree 6 [*Richards et al.*, 1988], suggesting that upwellings of different wavelengths can reproduce geoid highs. For example, the large-scale lower-mantle African and Pacific superswells [*Hager et al.*, 1985] and smaller-scale upper mantle Hawaii and Iceland hot spots [*Richards et al.*, 1988] both give rise to geoid highs. The Ross sea region maybe unique because it has a large geoid low located above both ancient subduction and possibly contemporaneous upwelling within the mantle.

[13] Residual bathymetry, obtained by subtracting an age-depth model from observed depths of ocean crust, indicates that a broad region between the ANT margin and the Pacific-Antarctic Rise is 500–1000 m shallower than expected (Figure 3b) [*Sutherland et al.*, 2010]. Bathymetric profiles perpendicular to the passive continental margins indicate that, although the shapes of the conjugate margins are nearly symmetric (Figure 3c), the ANT margin is ~1 km higher than the NZ margin [*Sutherland et al.*, 2010]. In addition, when the effects of sediment loading by up to 4 km of Late Cretaceous and Cenozoic postrift sediments is accounted for in five petroleum wells of the northern Campbell Plateau [*Cook et al.*, 1999], observed tectonic subsidence is 0.5–0.9 km larger than expected from reasonable rifting models [*Cook et al.*, 1999]. Excess subsidence occurred in the period 70–40 Ma, coincident with the phase of the rapid northward drift of New Zealand away from Antarctica, and significantly after the end of sedimentary basin formation [*Sutherland et al.*, 2010].

4. Methods

[14] We use CitcomS version 3.0, a finite element code for solving thermal convection within the mantle [*Tan et al.*, 2006; *Zhong et al.*, 2000] to develop global three-dimensional spherical models with assimilated plate motions. The plate velocities and plate polygons are defined at 1 Myr intervals (Gurnis et al., Global plate reconstructions with continuously closing plates, submitted to *Geochem. Geophys. Geosyst.*, 2009), and the velocity field is linearly interpolated for intervening times. We solve the equations of conservation of (1) mass, (2) momentum, and (3) energy for an incompressible, Newtonian fluid, while making the Boussinesq approximation:

$$\nabla \cdot \mathbf{u} = 0 \tag{1}$$

$$-\nabla P + \nabla \cdot \left[\eta \left(\nabla \mathbf{u} + (\nabla \mathbf{u})^{T}\right)\right] = \rho_m \alpha T \mathbf{g} \tag{2}$$

$$\frac{\partial T}{\partial t} = -\mathbf{u} \cdot \nabla T + \kappa \nabla^2 T + H \tag{3}$$

where $\mathbf{u}$ is velocity, P dynamic pressure, η dynamic viscosity, ρ_m ambient mantle density, α thermal expansion coefficient, $\mathbf{g}$ gravitational acceleration, T temperature, κ thermal diffusivity, and H internal heat production. Internal heating is negligible on the <100 Myr time scales studied here. Values of model parameters held constant are given in Table 1.

[15] Dynamic topography h on the top surface is defined as:

$$\sigma_{r,r} = (\rho_m - \rho_w) g h \tag{4}$$

where $\sigma_{r,r}$ is total normal stress in the radial direction, $\rho_m - \rho_w$ is the density contrast across top surface between water and mantle.

[16] Effective viscosities are temperature dependent according to:

$$\eta = \eta_0 \exp\left[\frac{E^*}{T + T_o} - \frac{E^*}{0.5 + T_o}\right] \tag{5}$$

where η is effective viscosity, η_0 is reference viscosity (Table 1), E^* is activation energy divided by the product of the gas constant R (8.314 J · K^{-1} · mol^{-1}) and temperature scaling T_S (3000 K), T is nondimensional

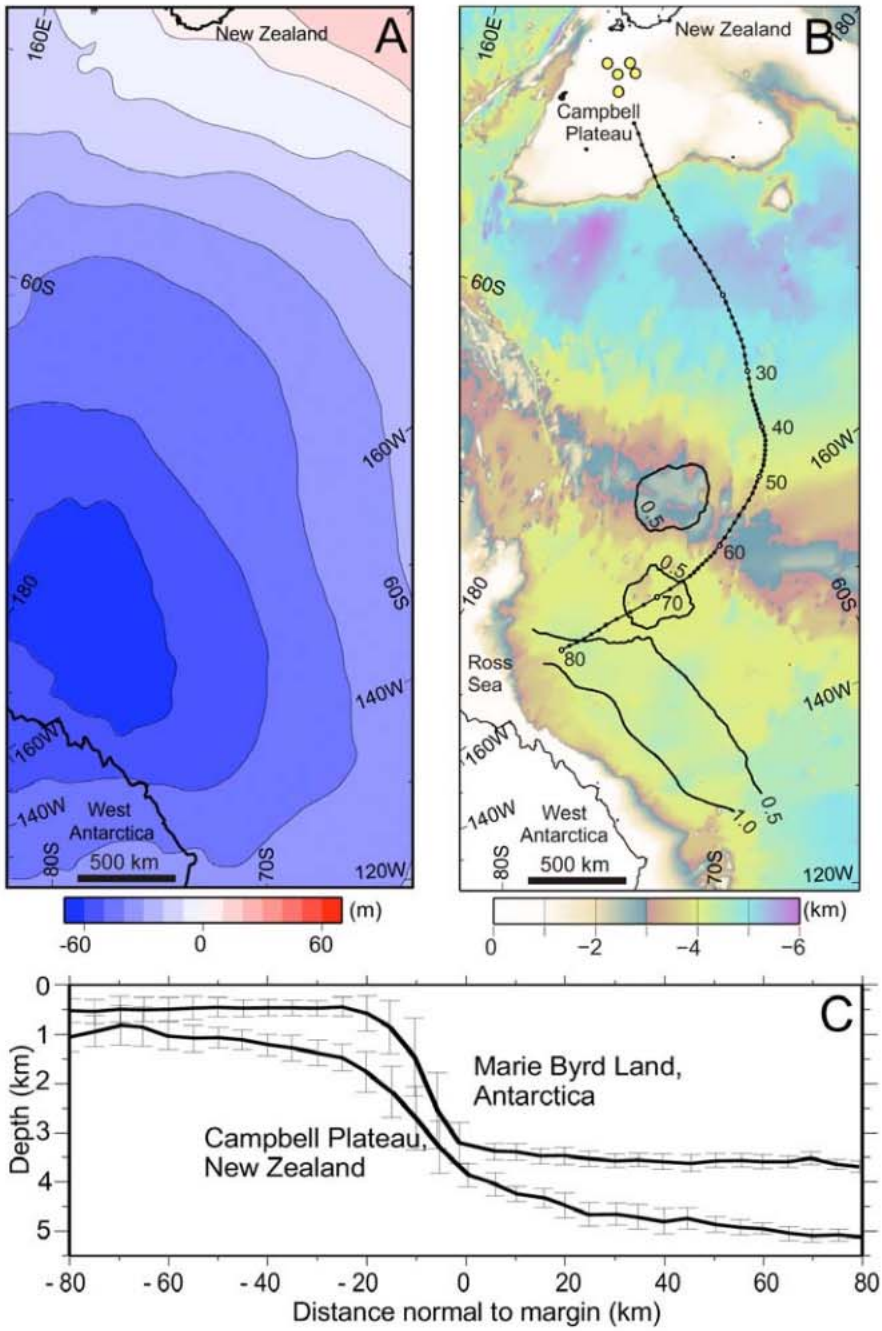

Figure 3. Observations used as constraints for our models. (a) Geoid [*Förste et al.*, 2008] with 10 m contour intervals. (b) Residual seafloor depth [*Sutherland et al.*, 2010], obtained after subtracting age-depth model with GEBCO bathymetry, showed with solid contour lines with 500 m contour intervals. Yellow dots show the position of five petroleum wells in Campbell Plateau, and the dotted line the relocated position of a point on the southern Campbell Plateau with respect to Marie Byrd Land since 80 Ma (1 Ma increments). (c) Bathymetry profiles [*Sutherland et al.*, 2010] perpendicular to Antarctica (145–160°W) and New Zealand margins (166–176°E), as a function of distance from the base of the Cretaceous continental margin, with bars indicating the standard deviation.

temperature, and T_0 is a temperature offset. We used values of $E^* = 1$ in the upper and $E^* = 5$ in the lower mantle, and $T_0 = 0.5$ for both upper and lower mantle, and these values correspond to relatively weak temperature dependence of viscosity.

[17] Except for initial discrete anomalies, the mantle is isothermal, with a nondimensional background temperature, $T_m = 0.5$. Top and bottom boundaries have mantle background temperature, and we do not impose thermal boundary layers. Because the study area is dominated by

Table 1. Model Parameters Held Constant in Our Runs

Parameter	Symbol	Value
Ambient mantle density	ρ_m	3340 kg/m^3
Water density	ρ_w	1000 kg/m^3
Reference viscosity	η_o	1×10^{21} Pa s
Thermal diffusivity	κ	10^{-6} m^2/s
Coefficient of thermal expansion	α	3×10^{-5} 1/K
Gravitational acceleration	g	9.81 m/s^2
Earth's radius	R	6371 km

divergent plate boundaries during its evolution, and has no active mantle plumes originating from the core-mantle boundary, such approximation is appropriate. We introduce upwelling anomalies $0.5 < T_U \leq 1$, and downwelling anomalies $0 \leq T_D < 0.5$, as oblate triaxial ellipsoids, with two long diameters (a and b) parallel to Earth surface and the shortest diameter (c) being vertical. Nondimensional maximum upwelling (downwelling) temperature is defined as $T_U = T_m + \Delta T_a$ ($T_D = T_m - \Delta T_a$), where ΔT_a is maximum nondimensional temperature of the anomaly. Temperatures in the ellipsoid follow Gaussian in all directions.

[18] The variables we attempt to constrain are: (1) geometry of buoyancy anomalies defined by ellipsoid diameters a, b and c, their depth (d_u and d_d) and geographic position initially at 80 Ma; (2) temperature anomalies ΔT_a; and (3) radial mantle viscosities, where we define a three-layer structure that includes lithosphere, upper mantle and lower mantle, with the lithosphere viscosity having constant value of 10^{23} Pa s. The top boundary layer is defined as a distinct high-viscosity rheological unit. For each model we define background viscosities for lower and upper mantle, which is modified by a temperature dependency in regions with thermal anomalies. All viscosity ratios reported are those between the background upper and lower mantle.

5. Model Results

5.1. Size and Position of Buoyancy Anomalies

[19] We first attempted to reproduce all observations in a time-dependent model with a single upwelling positioned immediately above a downwelling. The downwelling is designed to correlate with the high-seismic-velocity anomaly deep in the lower mantle (Figure 2). Although the high-velocity region may be the result of slab accumulation, we simplify the downwelling by introducing a single body with c = 800 km. The upwelling anomaly, located immediately above the downwelling at 80 Ma, with its lower edge 100 km from the upper edge of the downwelling, is designed to reproduce general features of the seismically low-velocity region at the end of calculation (0 Ma). The short diameter of the upwelling is varied between 500 and 800 km. The values of diameters a and b, and ΔT_a are assumed to be the same for both the upwelling and downwelling. We start all models at 80 Ma, roughly coincident with proposed initiation of ANT- Pacific spreading [*Stock and Molnar*, 1987; *Sutherland*, 1999a].

[20] The observed geoid and bathymetry anomaly constrain the size and position of the anomalies. If the initial size of the anomalies is too small or large, the predicted geophysical anomalies are spatially smaller or larger than observed. The long-wavelength extent and trend of the geoid and dynamic topography (Figure 3) are best reproduced with anomalous bodies that have longest diameter a approximately 4000 km, initially centered at 170°E and 75°S at 80 Ma. Since the observed anomalies are slightly elongated in the east-west direction (Figure 3), parallel to the Antarctica margin, we choose b = 3000 km. We tested a number of models with larger and smaller values of a and b, but they fail to reproduce the observed wavelengths.

5.2. Magnitude of Buoyancy Anomalies

[21] From the conservation of momentum and energy, dynamic topography in uniform viscosity and layered viscosity domain can be described as:

$$h(t) = C_1(t)\Delta T \quad (6)$$

$$h(t) = C_2(t)\frac{\eta_{UM}}{\eta_{LM}}\Delta T \quad (7)$$

where h is dynamic topography, ΔT is temperature anomaly, C_1 and C_2 are numerical functions obtained from the solution of flow and is dependent on the viscosity and temperature structure, and η_{LM} and η_{UM} are viscosities of lower and upper mantle, respectively [*Gurnis et al.*, 2000]. The nondimensional temperature anomaly is defined with respect to a temperature of 3000°C.

[22] Assuming the observed bathymetric anomaly (Figures 3b and 3c) can be attributed to dynamic topography, we use it to constrain the amplitude of the temperature anomaly. When we systematically vary the initial temperatures (Figure 4), while holding the initial depths (d_u = 1300 km and d_d = 2000 km) and viscosity ratio (η_{LM}:η_{UM} = 100:1) constant, small values of ΔT_a = 0.05 predict dynamic topography on order of only 100 m (Figure 4a), significantly less than the observed 500–1000 m. For large values of ΔT_a (0.2 and 0.3), the predicted maximum dynamic topography is on the order of 5 km, much larger than observed (Figures 4d and 4e). Observed present-day dynamic topography is reproduced with nondimensional temperatures of 0.1–0.15 (Figures 4b and 4c), with a best prediction of the geoid for ΔT_a = 0.15 (Figure 4c), and estimated error of 0.05.

[23] For large nondimensional temperatures of $\Delta T_a \geq 0.2$, the upwelling rises quickly, underplates the lithosphere, and overpredicts dynamic topography (Figures 4d and 4e). Models with $\Delta T_a \geq 0.2$ reproduce both regions of sublithospheric and transition zone-upper mantle high temperatures (Figures 4d and 4e), equivalent to the two low-seismic velocity regions evident in tomography. However, we find that dynamic topography is significantly overpredicted for all models with $\Delta T_a \geq 0.2$ and all models in which the main mantle upwelling underplates the lithosphere. Only when the main large upwelling ends up within the transition zone-upper lower-mantle depth range (Figures 4b and 4c; ΔT_a = 0.1–0.15), can we successfully match residual bathymetry (Figure 3b), regardless of the initial depth or mantle viscosities.

[24] There is a trade-off between the magnitude of the temperature anomaly and the mantle viscosities (equation 7). We iteratively varied ΔT_a and mantle viscosities, and found that ΔT_a in range of 0.1–0.15 always best predicted dynamic topography. For all subsequent results, we fixed ΔT_a to 0.15,

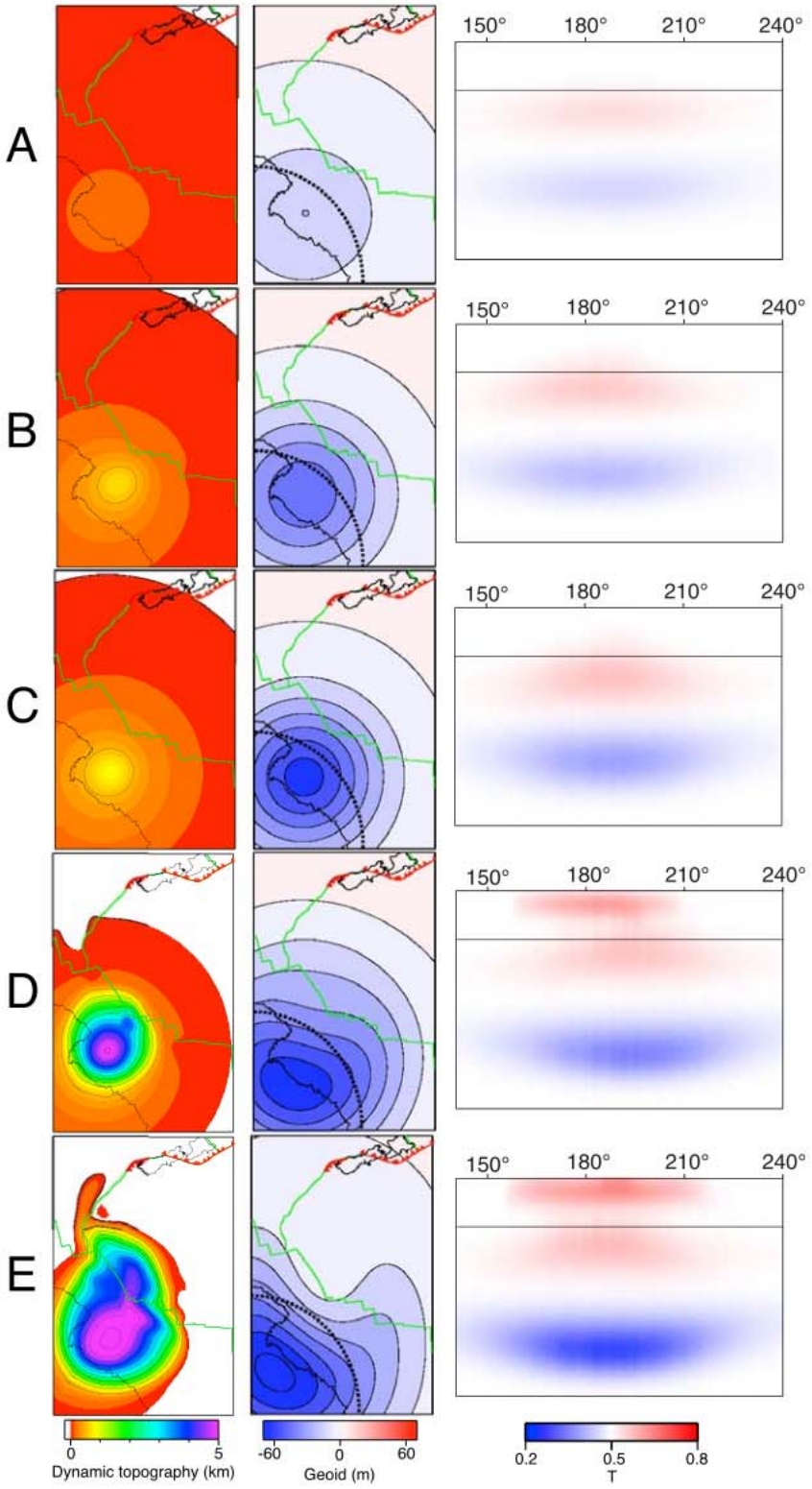

Figure 4. Constraining temperature anomaly based on predictions of dynamic topography (500 m contour interval), geoid (10 m contour interval), and upwelling geometry at 0 Ma for $\mathbb{D}\ T_a$ of (a) 0.05, (b) 0.10, (c) 0.15, (d) 0.20, and (e) 0.30. Green lines indicate position of mid-ocean ridges, red lines with triangles subduction zones, and dotted black lines indicate location of cross sections. Cross sections show whole mantle depth range, with position of 660 km discontinuity shown with horizontal black line.

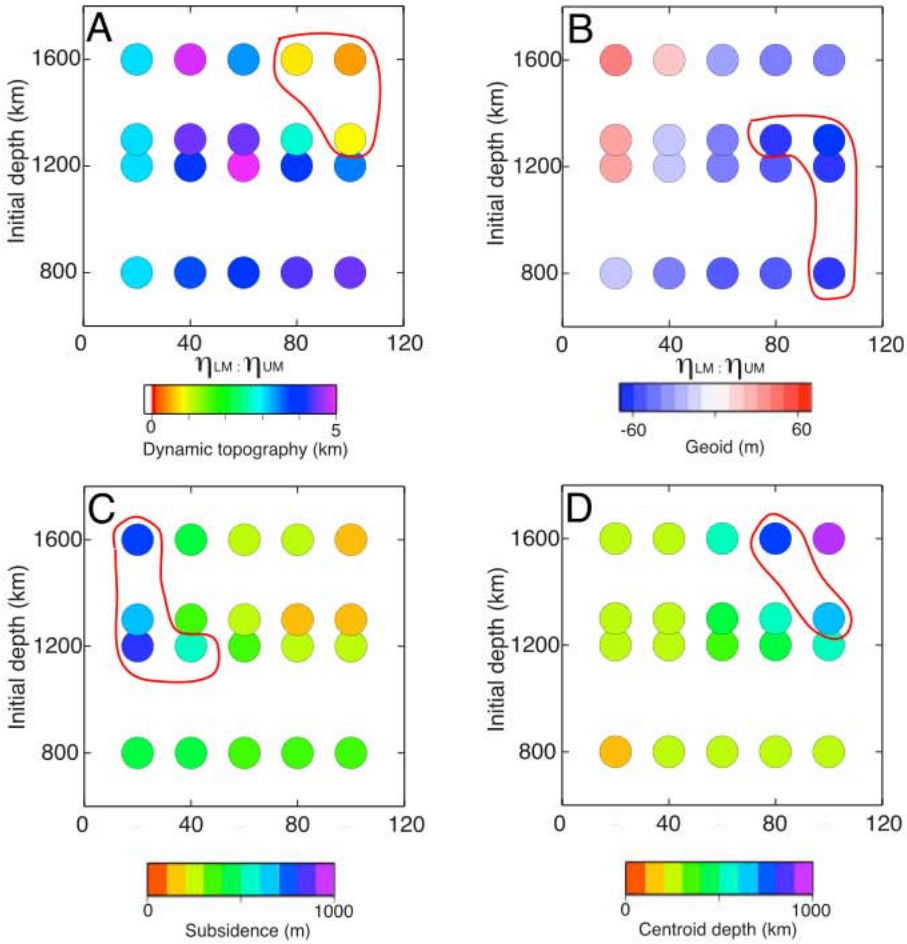

Figure 5. Constraining relative mantle viscosity ratio h_{LM}:h_{UM} and initial depth of upwelling anomaly utilizing (a) dynamic topography, (b) geoid, (c) subsidence, and (d) centroid depth of main upwelling anomaly at 0 Ma as constraints. Red outlines indicate set of models satisfying individual constraints. Relative ratios are given with respect to background viscosity of 10^{21} Pa s.

while noting a slight trade-off with other parameters if a slightly lower temperature is chosen.

5.3. Mantle Viscosity Structure and Initial Upwelling Depths

[25] Once we fix the geometry and amplitude of the temperature anomalies, which define the buoyancy forces, a trade-off remains between the initial anomaly depth and mantle viscosity. We systematically varied the ratio of h_{LM}:h_{UM} and the initial depth of anomalies at 80 Ma (Figure 5), with the model setup described in section 3.1 and $\mathrm{D}\,T_a$ = 0.15. In addition to comparing predicted and observed geoid, present-day dynamic topography and Campbell Plateau subsidence history, we also compare the predicted final geometry of the high-temperature anomaly with that of the observed midmantle low-velocity anomaly (central depth approximately 700 km), to further constrain plausible initial depths for the anomaly and the mantle viscosity structure.

[26] All models with h_{LM}:$h_{UM} \leq 60$ significantly overpredict dynamic topography (Figure 5a), reproduce either positive or small negative geoid anomalies (Figure 5b), and result in shallow centroid depths of the upwelling anomaly at 0 Ma (Figure 5d). The upwelling rises relatively quickly with lower viscosities, underplating the lithosphere and overpredicting dynamic topography, similar to models with $\mathrm{D}\,T_a \geq 0.2$. Dynamic topography is also overpredicted when the initial depths d_u are shallower than 1300 km (Figure 5a), while the geoid is under predicted or has the wrong sign when d_u is deeper than 1300 km (Figure 5b). Final centroid depths are less than 500 km for all models with initial d_u of 800 km and 1200 km.

[27] Present-day observations of dynamic topography and geoid, and appropriate midmantle centroid anomaly depths are simultaneously reproduced with a single model in which d_u is 1300 km and the viscosity ratio h_{LM}:h_{UM} is 100. However, the fit to subsidence is only reproduced when h_{LM}:$h_{UM} \leq 40$ (Figure 5c). We found that no model with a single upwelling and downwelling could reproduce all observations, even when the parameter range was expanded beyond that shown in Figure 5. This indicates that our assumed initial geometry of the buoyancy anomalies must be unrealistic, and that a more complex parameterization of initial conditions may be needed to match all observations.

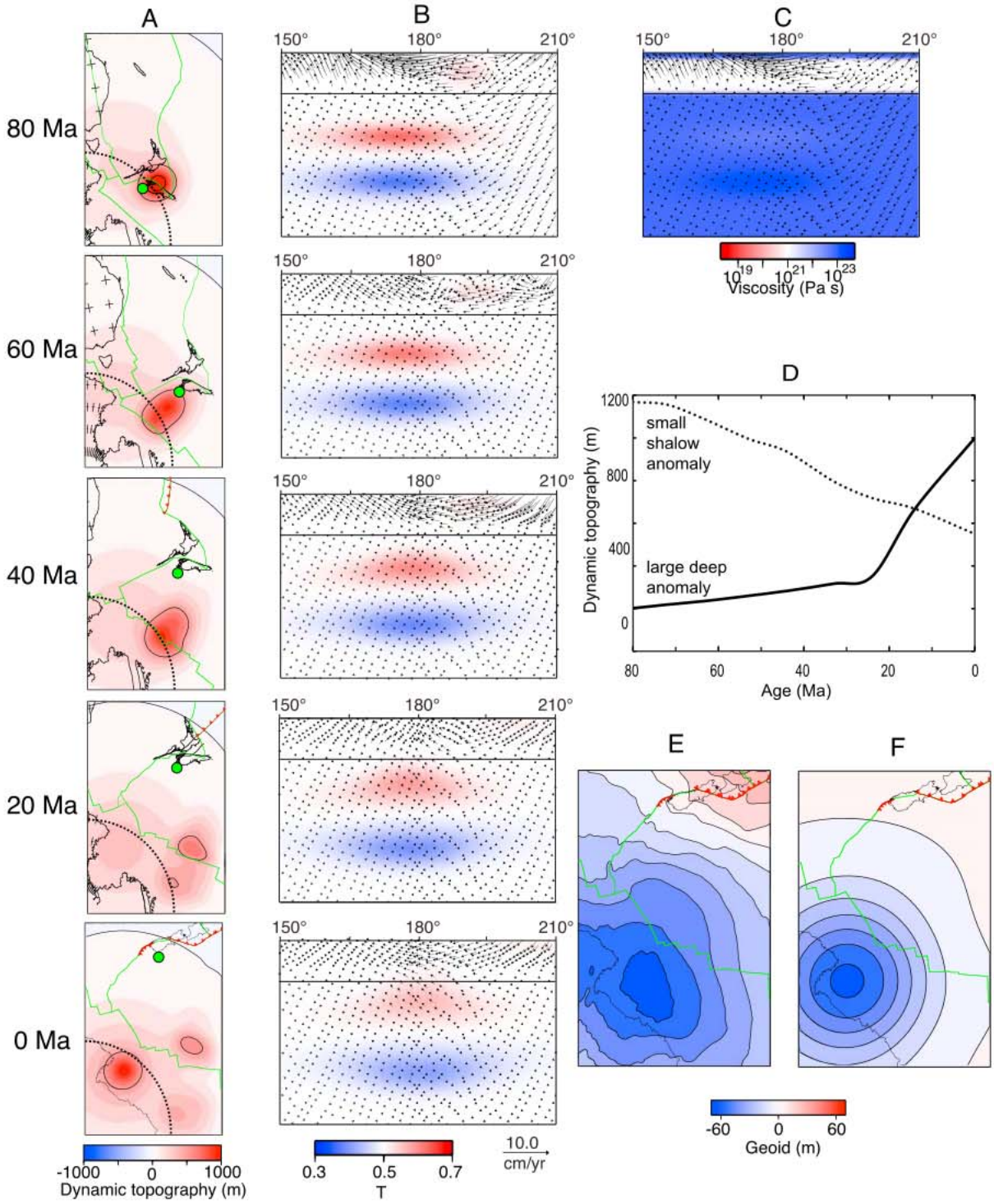

Figure 6. Modeling results for a model with two hot anomalies evolving above a cold anomaly (h_{LM}:h_{UM} = 100:1, with respect to viscosity of 10^{21} Pa s). (a) Dynamic topography predictions (500 m contour interval). (b) Cross sections of temperature field at 70°S with velocity vectors overlain. (c) Cross section of viscosity field at 70°S and 80 Ma with velocity vectors overlain. (d) Evolution of the maximum amplitude of dynamic tomography over the smaller shallow upwelling (dotted line) and the main large upwelling (solid line). (e) Geoid observation [*Förste et al.*, 2008]. (f) Geoid model predictions. Green lines indicate position of mid-ocean ridges, red lines with triangles subduction zones [*Gurnis et al.*, 2009], and dotted black lines indicate location of cross sections. Cross sections show whole mantle depth range, with position of 660 km discontinuity shown with horizontal black line (Figure 6b) or discontinuity in viscosity field (Figure 6c). The reconstructed location of Campbell Plateau is shown with green dot (Figure 6a).

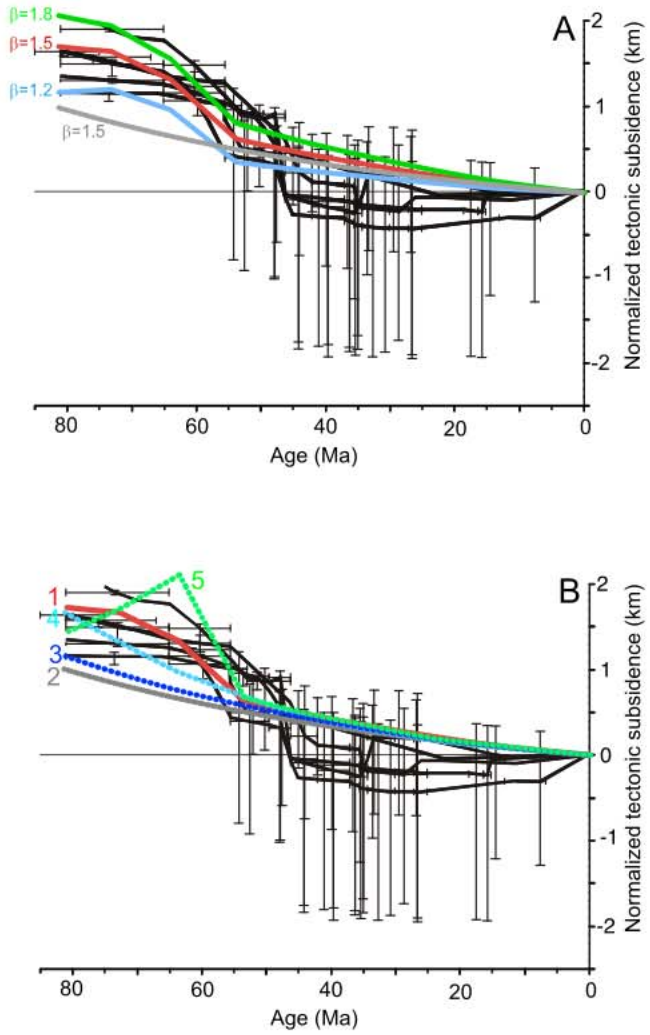

Figure 7. Tectonic subsidence of the Campbell Plateau. (a) Tectonic subsidence for five wells (black lines) compared with thermal subsidence only (gray line) and thermal+dynamic subsidence for β = 1.2 (blue line), β = 1.5 (red line), and β = 1.8 (green line). (b) Comparison between tectonic subsidence prediction between (1) the best model described in section 5.4, (2) thermal subsidence model with β = 1.5, (3) model with a single hot anomaly rising from initial depth 1300 km in a mantle with h_{LM}:h_{UM} = 100:1, (4) model with a single hot anomaly rising from depth of 1600 km in a mantle with h_{LM}:h_{UM} = 20:1, and (5) model with additional shallower anomaly with rising from central depth of 500 km and ΔT_a = 0.11. Error bars indicate uncertainty in determining paleowater depths.

5.4. More Realistic Initial Conditions With a Second Upwelling

[28] In order to match the history of Campbell Plateau subsidence and observations of the modern topography, geoid, and tomography, we introduce an additional shallower low-density anomaly in the upper mantle below the reconstructed position of the Campbell Plateau at 80 Ma (Figure 6). The location is slightly closer to the surface trace of subduction and would be consistent with an additional shallow upwelling above a south-dipping slab that was subducted at the northern margin of the NZ continent [*Davy et al.*, 2008].

[29] The best fitting model has an additional hot anomaly with $a = b$ = 1500, c = 500km, depth 500 km and ΔT_a = 0.08, and its center is located at 160°W and 68°S at 80 Ma, approximately 1200 km NE from the center of the main anomaly. The predicted Campbell Plateau dynamic topography for this model at 80 Ma is about 750 m (Figure 6a), with the maximum located on the NW part of the Campbell Plateau. As ANT-NZ seafloor spreading progressed, the Campbell Plateau (NZ) drifted northward with respect to ANT and the lower mantle (Figure 6a), and moved across the region of high dynamic topography. By 40 Ma, the Campbell Plateau had moved completely away from the dynamic topography high. As the larger and deeper upwelling arose from the lower mantle, it produced increased dynamic topography in the Ross Sea, reaching about 1000 m presently (Figure 6a). The smaller and shallower upwelling was split as the spreading ridge passed over the anomaly during the Cenozoic (Figure 6a), producing secondary dynamic topography highs with maximum amplitudes of about 600 m on either side of the Pacific-Antarctic ridge. The model ridge topography (Figure 6a) matches observed bathymetry along the spreading ridge (Figure 3b). Dynamic topography associated with the shallow anomaly is dominant for most of the model history (Figure 6d), with the effect of the deep-seated anomaly significantly increasing after 20 Ma, and reaching up to 1000 m at the present (Figure 6d). The main upwelling in the model reached the upper mantle at about 20 Ma (Figure 6b), and is now located at 400–1000 km depth, where it matches the low-seismic-velocity anomaly at the transition zone and top of the lower mantle (Figure 2). The smaller upwelling spread out beneath the oceanic lithosphere (Figure 6b), where it matches the sublithospheric region of extremely slow seismic velocities (Figure 2).

[30] The present-day geoid anomaly predicted by this model is −62.5 m (Figure 6f), which is close to the known amplitude (Figure 6e). Considering the simplified geometry and parameterization of our model, the predictions match the general wavelength and location of geoid and topography anomalies well. The amplitude and sign of the geoid are primarily controlled by both the depth of the deep-seated upwelling anomaly at 0 Ma and the relatively large ratio of upper to lower-mantle viscosities.

[31] When we track dynamic topography of the Campbell Plateau (Figure 6a) from 80 to 0 Ma, we calculate the total excess subsidence of the Campbell Plateau is 750 m, which mostly results from the northward drift of the Campbell Plateau away from the upwelling. For comparison, when we attempt to match the observed tectonic subsidence of the Campbell Plateau with a stretching model alone (no dynamic topography), the subsidence is under predicted by 500–900 m (Figure 7a, gray line). When the predicted dynamic topography is added to a model of thermal subsidence (Figure 7a), the total observed tectonic subsidence is well matched by assuming a stretching factor β = 1.5, which is a typical value estimated from crustal thickness or fault heaves from near to the wells that were considered [*Cook et al.*, 1999]. The maximum predicted subsidence rate occurs around 60 Ma, coincident with an observed transition from shallow to deep-water environments in the wells

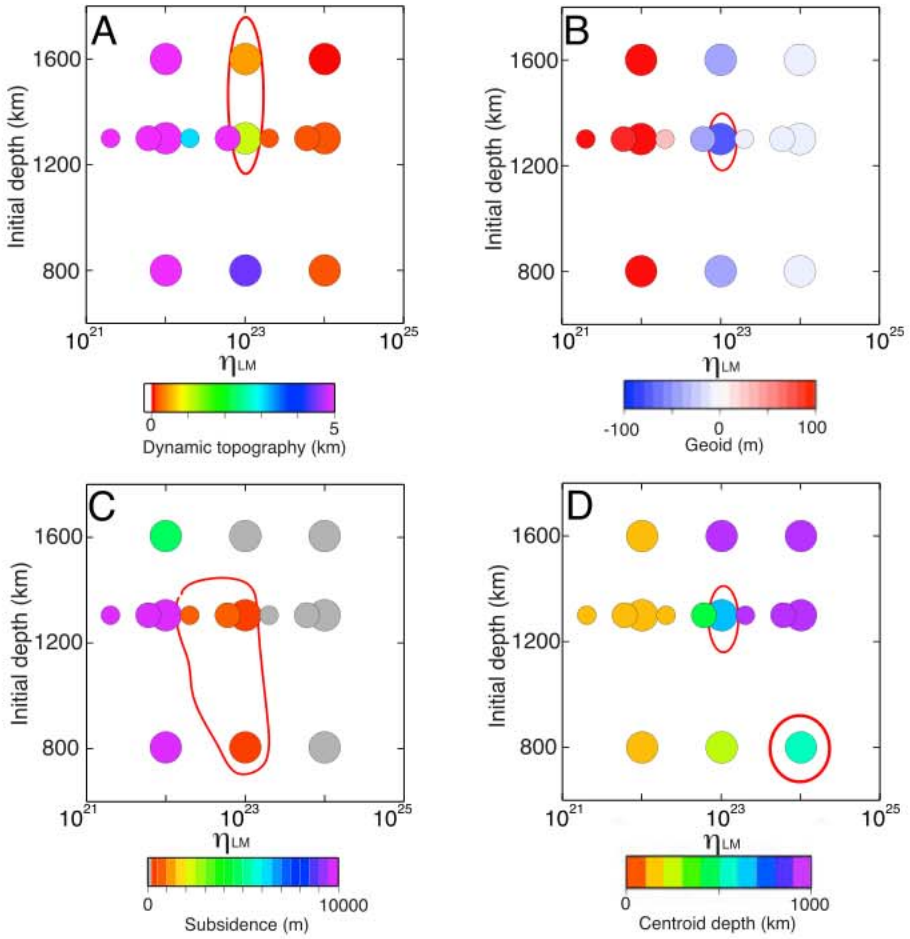

Figure 8. Constraining absolute mantle viscosity and initial depth of upwelling anomaly utilizing (a) dynamic topography, (b) geoid, (c) subsidence, and (d) centroid depth of upwelling anomaly at 0 Ma as constraints. The largest circles indicate models with η_{LM}:η_{UM} = 100:1, intermediate circles models with η_{LM}:η_{UM} = 60:1, and the smallest circles with η_{LM}:η_{UM} = 20:1. Red outlines indicate set of models satisfying individual constraints.

(Figure 7a), and it resulted from the drift of the Campbell Plateau away from the upwelling (Figure 6a).

[32] Models with a single large mantle upwelling centered at the ANT margin always under-predict Campbell Plateau tectonic subsidence (Figure 7b, blue and cyan curves), and never reproduce the observed inflexion in subsidence rate. Models in which a smaller secondary upwelling anomaly is located slightly deeper at 80 Ma and with a higher-amplitude temperature anomaly, could reproduce the total amplitude of tectonic subsidence, but the shape of the predicted subsidence curve fits the observations slightly worse (Figure 7b, green curve). The exact shape and amplitude of the Campbell Plateau subsidence curves is strongly controlled by the movement of the plateau with respect to the dynamic topography high (Figure 6d), so several models with different initial geometries and ΔT_a of the smaller hot anomaly could reproduce observations equally well, because observations have poor spatial coverage.

5.5. Absolute Values of Mantle Viscosities

[33] Instantaneous mantle convection models with seismic tomography, geoid and/or dynamic topography as constraints [e.g., *Hager*, 1984; *King and Masters*, 1992; *Steinberger and Calderwood,* 2006] can be used to derive a radial relative viscosity profile, while postglacial rebound observations are used to derive absolute viscosities [e.g., *Milne et al.*, 2004; *Mitrovica and Forte*, 2004]. We show above that observations of geoid and dynamic topography in the ANT-NZ region require a high η_{LM}:η_{UM} ratio of about 100:1 (Figure 5). However, since we have observations of tectonic subsidence as a function of time and seismic tomographic models constrain the present depths of buoyancy anomalies, we can also constrain absolute viscosities within the mantle. For our best fitting model (section 5.4), which includes two hot anomalies at different depths, we systematically vary the absolute value of lower-mantle viscosity for models with d_u (depth to larger hot anomaly) of 800, 1300, and 1600 km (Figure 8).

[34] For models with $\eta_{LM} \leq 10^{22}$ Pa s, the hot anomaly rises too quickly, underplates lithosphere by 0 Ma (Figure 8d), overpredicts dynamic topography (Figure 8a) and subsidence (Figure 8c), while yielding positive geoids (Figure 8b). If the lower-mantle viscosity is higher, with η_{LM} of 10^{24} Pa s, the upwelling anomaly rises more slowly,

generally resulting in large centroid depths of midmantle anomaly at 0 Ma (Figure 8d), while under predicting dynamic topography (Figure 8a), the geoid (Figure 8b) and dynamic subsidence (Figure 8c). For a narrow range of lower-mantle viscosities $\eta_{LM} = 2 \times 10^{22}$ to 1×10^{23} Pa s, dynamic topography is close to the observed 0.5–1.0 km for depths $d_u < 1600$ km (Figure 8c). Observations of dynamic topography and geoid (Figures 8a and 8b) require lower-mantle viscosity $\eta_{LM} = 10^{23}$ Pa s, and only depths close to $d_u = 1300$ km yield acceptable predictions for all observations. Although a model with the shallow upwelling (800 km) and stiff lower mantle ($\eta_{LM} = 10^{24}$ Pa s) produces reasonable midmantle centroid upwelling depths compared to seismic tomography (Figure 8d), the model underestimates all other parameters (Figures 8a–8c).

6. Discussion

6.1. Mantle Dynamics and Viscosity Structure

[35] We can fit both the present-day (geoid, dynamic tomography, and seismic structure) and time-dependent (tectonic subsidence of Campbell Plateau) observations in a single dynamic model with a relatively simple initial geometry and viscosity structure. We define thermal anomalies as triaxial ellipsoids that are designed to reproduce the large-scale characteristics of mantle flow and evolution, rather than to match the exact shape and extent imaged in seismic tomography. In reality, these anomalies certainly have a more complex geometry, but since tomography models differ significantly in their detail of midmantle and lower-mantle seismic-velocity structure [*Grand*, 2002; *Gu et al.*, 2001; *Masters et al.*, 2000; *Ritsema and van Heijst*, 2000], we choose to use simplified forward models designed to match the general geometrical characteristics and depth ranges of the largest anomalies. When the resolution and coverage of tomography models in the Antarctica-New Zealand region are improved, it will be possible to better separate and define the position and shape of the velocity anomalies of interest (in particular the midmantle velocity low and lower mantle velocity high), and seismic properties could then be used as input to inverse models that have a more complex parameterization [e.g., *Liu et al.*, 2008]. We also simplify the definition of the boundary layers in a way that is appropriate for the tectonic setting. The top boundary layer is treated as a layer with a high viscosity, with the temperature being equal to the background mantle temperature. This formulation is appropriate since the study region is dominated by divergent boundaries during the whole model history, and the buoyancy anomalies were dominated by advection below the lithosphere when the model results were compared with the observations. A bottom thermal boundary layer is also neglected because the region since the Late Cretaceous was dominated by a large downwelling associated with subducted Gondwana slabs without any active plumes rising from the core-mantle boundary.

[36] On the basis of the spatial scale of the Ross sea geoid and topography anomaly, we define the largest (one hot and one cold) buoyancy anomalies to have lateral and vertical dimensions of 4000 km and 600–800 km, respectively. On the basis of our fit to the observed present-day dynamic topography and geoid, we determine a maximum temperature anomaly of approximately 450°C, giving an average temperature anomaly within the rising upwelling of about 200°C. On the basis of direct conversion of seismic velocities to thermal anomalies, maximum temperature anomalies have previously been estimated to be +600°C at 1400 km depth beneath the Ross Sea, and -400°C at 2800 km depth [*Deschamps and Trampert*, 2003]. The global average of temperature variability is estimated to be approximately 190°C at 1400 km depth [*Deschamps and Trampert*, 2003], while temperature anomalies close to the CMB could reach as much as 900°C [*Deschamps and Trampert*, 2003; *Forte and Mitrovica*, 2001]. Accounting for both a thermal and compositional origin for tomographic anomalies, temperature variation is estimated to be between 200°C [*Karato and Karki*, 2001] and 300°C [*Deschamps and Trampert*, 2003] for upper parts of the lower mantle; and 300–400°C for midmantle [*Deschamps and Trampert*, 2003]; and 500°C [*Deschamps and Trampert*, 2003] to more than 1000°C [*Karato and Karki*, 2001] for the lowermost mantle. Although the temperature anomaly we infer is in the range of values suggested by these studies, it should be noted that we assume that the entire upwelling/downwelling anomaly is thermal. It is possible that a part of the buoyancy we infer is compositional, which could result in lower estimates of temperature anomalies beneath the ANT margin. If the anomalies were entirely thermal in origin, the corresponding average density difference between the anomaly and the ambient mantle would be about 0.6%. In addition, we use a constant coefficient of thermal expansion (Table 1). If a depth-dependent coefficient was used, we would have obtained different estimates of thermal anomaly, but the estimated value of density anomaly would remain unchanged.

[37] By simultaneously introducing instantaneous and time-dependent observations, we are able to infer both relative and absolute mantle viscosities for the assumed initial geometry. Seismic tomography provides information on the present-day distribution of mantle heterogeneity, and is the result of the history of mantle flow. The lower to upper mantle viscosity ratio that we find is best able to fit all observations is about 100:1, with present-day dynamic topography and geoid giving the strongest constraints. Time-dependent observations impose important constraints on the absolute value of the viscosities, with a lower-mantle viscosity of 10^{23} Pa s and an upper mantle viscosity of 10^{21} Pa s giving the most acceptable fits. A stiffer mantle, having lower-mantle viscosity higher than 10^{23} Pa s, results in underestimated dynamic topography, geoid and tectonic subsidence, with an overestimated final depth of buoyant anomalies. A less viscous mantle, with lower-mantle viscosity being smaller than 10^{23} Pa s, results in a relatively rapid rise of anomalies, overpredicting tectonic subsidence and dynamic topography, while having final depth of hot anomaly too shallow. The best initial depth of the large upwelling anomaly in our models is around 1300 km. When individual observational constraints are imposed separately, we find a trade-off between initial depth and viscosity, where deep anomaly/less viscous mantle can give an equally well-constrained prediction as shallow anomaly/more viscous mantle. However, when the observations are used jointly, a narrower range of possible mantle viscosities and anomaly depths are found.

[38] Absolute viscosities can be independently obtained by inversion of postglacial rebound rates [*Milne et al.*, 2004] or joint inversion of convection and glacial isostatic adjustment [*Mitrovica and Forte*, 2004]. Our preferred absolute lower-mantle viscosity (10^{23} Pa s) is higher than values obtained by inversion of Fennoscandian GPS data [*Milne et al.*, 2004], while it fits well within the range of the values inferred by [*Mitrovica and Forte*, 2004]. Instantaneous flow models [e.g., *Hager*, 1984; *King and Masters*, 1992; *Steinberger and Calderwood*, 2006] constrained by the geoid are consistent with a jump of viscosities across the 660 km discontinuity higher than 30, and possibly as high as 100. Therefore, our estimate of a jump at the base of the transition zone by a factor of 100 corresponds to the higher-end estimate obtained from instantaneous models. Our preferred value of relative viscosity ratio is significantly higher than h_{LM}:h_{UM} = 15:1 obtained in an adjoint mantle convection model of North America, constrained by seismic tomography, stratigraphy and plate motion [*Liu et al.*, 2008; *Spasojevic et al.*, 2009]. In addition, our estimated lower-mantle viscosity is an order of magnitude larger than ~10^{22} Pa s obtained by analytical calculations on the basis of sinking velocities of a subducted fossil slab in Tasman Sea [*Schellart et al.*, 2009]. Differences in the ratio of mantle viscosities inferred by different geodynamic studies could partly be explained by global lateral variations in viscosity. The high-viscosity ratio of 100 determined in this study could be related to the long history of subduction that accumulated cold material in the lower mantle, resulting in larger thermally controlled viscosity contrasts between the upper and lower mantle, and the subduction history may also have regionally altered mantle chemistry. In addition, it should be noted it is possible that these upwelling anomalies are created in a more continuous process, in which upwellings are continuously fed by a process (e.g., slab dehydration), such that there is a constant influx of lower density material. We do not have ability to model such a process and we devised a simplified model in which upwelling with a shape defined at 80 Ma evolves to the present. If we had ability to model a more continuous process, it is possible that estimated values of mantle viscosities would be different.

[39] The correct sign and amplitude of the geoid could be reproduced only when the large-scale main upwelling is now positioned in the transition zone and top of the lower mantle. Since other mantle upwellings, such as the African superswell and the Iceland and Hawaii plume, are associated with large geoid highs [*Richards et al.*, 1988], the Ross sea region appears to be rather unique. Geoid dynamic response functions [*Hager*, 1984; *Richards and Hager*, 1984] for a range of wavelengths suggest that both buoyant upwellings in the transition zone and dense slabs in the lower mantle could produce geoid lows, if the viscosity of the upper mantle is significantly less than that of the lower mantle. Alternatively, response functions for a long-wavelength upwelling located in the lower mantle (e.g., African superswell), or a shorter-wavelength anomaly located in the upper mantle (e.g., Hawaii or Iceland), predict a positive geoid response, assuming an appropriate viscosity contrast [*Richards and Hager*, 1984]. Our models demonstrate that the Ross Sea geoid low can be attributed to sharper mantle viscosity gradients and/or the intermediate wavelength of the upwelling at midmantle depths.

6.2. Regional Geologic and Tectonic Implications

[40] Our models were constructed only to fit observations of modern topography, geoid, and seismic-wave speed anomalies, and the 80–0 Ma subsidence history of the Campbell Plateau. However, the models make indirect implications for other geologic observables, such as the composition of the mantle and derived melts through time. In addition, the very basic conclusion that such a class of model with upwellings and a downwelling is required by the regional geology and geophysics is worthy of discussion.

[41] The tectonic subsidence histories that we predict are derived from tracking a point on the surface of the Pacific plate as it moved northward across the upper boundary of evolving mantle flow. The shallower and smaller of the discrete upwellings that we infer was initially located beneath the reconstructed Campbell Plateau at 80 Ma, where it created a long-lived dynamic topography high that we infer to be partially responsible for anomalously shallow depths to the Pacific-Antarctic Rise and adjacent seafloor to Marie Byrd Land. As the Campbell Plateau moved northward, it experienced subsidence as it moved off the dynamically supported high. In contrast, the Australian and North American continents are shown to have experienced tectonic subsidence as they moved across mantle downwellings associated with relict slabs [*Gurnis et al.*, 1998; *Spasojevic et al.*, 2009]. Our study further demonstrates that understanding the evolution of mantle flow beneath sedimentary basins is fundamental to predicting their subsidence histories.

[42] We have not attempted to model all the known subsidence histories from around New Zealand, which are complicated by development of the Cenozoic Australia-Pacific plate boundary. However, we suggest it is significant that paleoenvironments inferred for most sedimentary basins around New Zealand were nonmarine at ~85 Ma [*Cook et al.*, 1999; *King et al.*, 1999; *Laird and Bradshaw*, 2004]. It is significant because rifting was already complete and crustal thickness was typically in the range 20–30 km, so global experience and comparison with the modern setting suggest that it should have been at or below sea level in the absence of dynamic topography associated with mantle flow. The widespread erosion surface that resulted from having an elevation above sea level was called the "Waipounamu Erosion Surface" by *LeMasurier and Landis* [1996] and was inferred by them to have been caused by dynamic topography.

[43] The conclusion that Late Cretaceous dynamic topography existed in southern NZ is implicit in the observed rapid subsidence of the Campbell Plateau during the interval 70–40 Ma, as it moved off the elevated region. This is the reason why we had to introduce an additional shallow mantle upwelling at 80 Ma below NZ (further north of the main deeper upwelling). We are not able to determine the precise pattern of mantle upwelling in the Late Cretaceous beneath southern NZ, owing to the sparse observations, but we can constrain the source to have been relatively shallow (transition zone or upper mantle).

[44] Three general classes of upwellings and hence hot spots have previously been identified [*Courtillot et al.*, 2003]: (1) upwellings that originate from the CMB region, (2) upwellings originating from the bottom of the transition

zone, and (3) upper mantle plumes, but the upwellings we propose do not correspond to any of the previously identified types. While specific phase transitions may lead to a layered viscosity and density structure and hence to certain modes of plume behavior, we suggest that the role of subduction in the genesis of instabilities that lead to upwelling may have been overlooked [*Sutherland et al.*, 2010]. Slabs that pass through the transition zone may sequester H_2O in superhydrous B [*Ohtani et al.*, 2003] or D phases [*Hirschmann*, 2006]. *Ohtani et al.* [2004] suggest that decomposition of superhydrous phases could occur at depths as large as 1250 km, resulting in hydration and/or melting of the mantle. Therefore, it is possible that the seismic low-velocity region imaged in the midmantle below the Antarctic-New Zealand region has been created by chemical and/or hydration reaction of mantle with subducting slabs below 660 km depth. If such a process is continuously active during subduction, it is possible that buoyancy anomalies have been created continuously, extending from midmantle depths to the surface. Buoyant material may be released to become upwellings when changes in subduction rate or the termination of subduction occurs and the competing downward force is reduced [*Sutherland et al.*, 2010]. The predicted correlation between reduction in subduction rate and subsequent mantle upwelling could be tested by analysis of the geologic record from ancient subduction systems for which it is possible to compute the past subduction rate.

[45] Tests of the plume generation hypothesis presented above may rest with the details of the geochemistry of mantle-derived rocks. It is outside of our present scope to explore this subject in detail, but we do present a few relevant observations from the NZ-ANT region. Cretaceous igneous rocks from New Zealand have high U/Pb mantle (HIMU) isotopic signatures, interpreted to be plume-related, but Antarctic rocks do not [*Mukasa and Dalziel*, 2000; *Weaver et al.*, 1994]. In contrast, Late Cenozoic mafic igneous rocks are widespread in the Ross Sea and Marie Byrd Land and do have geochemistry that falls on a HIMU trend [*Behrendt et al.*, 1991; *Finn et al.*, 2005; *Rocchi et al.*, 2002]. Superficially, this seems in excellent agreement with the general characteristics of our models. However, to test the plume generation model that we propose requires a specific geochemical prediction from the model, and an understanding of the inherited geochemistry of the mantle, and of the lithospheric processes and chemical history near the sample site. A HIMU descriptor may not be optimal or appropriate. We conclude that initial interpretations support our models, but we leave the development of this discussion to more detailed future study.

7. Conclusions

[46] Anomalous geophysical observations at NZ-ANT margin can be reproduced with a dynamic model in which two hot anomalies evolved above a cold downwelling related to Gondwana subduction. The main larger hot mantle anomaly, centered above the Ross sea region, originates from a midmantle depth range of 1000–1600 km at 80 Ma, and has an average temperature approximately 200°C higher than the background mantle. If the anomalies were thermal in origin, the corresponding average density variation between the anomaly and background mantle would be about 0.6%. This buoyant anomaly reached the upper mantle at ~20 Ma, and it evolved to a present-day depth range of 400–1000 km, resulting in up to 1 km of dynamic topography that is now observed along the ANT margin.

[47] Campbell Plateau subsidence and present-day residual bathymetry of the Antarctica-Pacific ridge is related to evolution of an additional hot anomaly, located at 80 Ma in the upper mantle, and which has now underplated the lithosphere to form a shallow seismic low-velocity anomaly. The mantle upwelling creates a long-lived dynamic topography high, and the anomalous Campbell Plateau subsidence was a result of northward drift away from this dynamic topography high.

[48] By using present-day (geoid, dynamic topography and seismic tomography) and time-dependent (tectonic subsidence) observations, we are able to infer both relative and absolute mantle viscosities. The relative viscosity ratio is rather high, with η_{LM}:η_{UM} = 100:1, and the steep gradient of the viscosities could be created by long-lived Gondwanaland subduction that resulted in an extensive pile-up of denser and more viscous material in the lower mantle that is overlain by a region of hydration. The absolute viscosities of the upper and lower mantle in the NZ-ANT region are 10^{21} and 10^{23}, respectively.

[49] The Ross sea geoid low could be reproduced only when the large-scale main upwelling anomaly is positioned across the transition zone and top of the lower mantle. This globally significant geoid low is reproduced in our model through a combination of the intermediate wavelength of upwelling and the high gradient of mantle viscosity.

[50] **Acknowledgments.** All calculations carried out on the Caltech Geosciences Supercomputer Facility were partially supported by NSF EAR-0521699. This work was supported through the New Zealand Foundation for Research Science and Technology, the Caltech Tectonics Observatory (by the Gordon and Betty Moore Foundation), the National Science Foundation (EAR-0609707 and EAR-0810303), StatoilHydro, and an ExxonMobil Science grant (to S.S.). The original CitcomS software was obtained from Computational Infrastructure for Geodynamics (http://geodynamics.org). This is contribution 10023 of the Division of Geological and Planetary Sciences and number 99 of the Tectonics Observatory, Caltech.

References

Adams, C. J., H. J. Campbell, and W. L. Griffin (2007), Provenance comparisons of Permian to Jurassic tectonostratigraphic terranes in New Zealand: Perspectives from detrital zircon age patterns, *Geol. Mag.*, *144*, 701–729, doi:10.1017/S0016756807003469.

Allmendinger, R. W., T. E. Jordan, S. M. Kay, and B. L. Isacks (1997), The evolution of the Altiplano-Puna plateau of the central Andes, *Annu. Rev. Earth Planet. Sci.*, *25*, 139–174, doi:10.1146/annurev.earth.25.1.139.

Behrendt, J. C., W. E. LeMasurier, A. K. Cooper, F. Tessensohn, A. Trefu, and D. Damaske (1991), Geophysical studies of the west Antarctic rift arm, *Tectonics*, *10*, 1257–1273, doi:10.1029/91TC00868.

Bina, C. R., and G. Helffrich (1994), Phase-transition Clapeyron slopes and transition zone seismic discontinuity topography, *J. Geophys. Res.*, *99*, 15,853–15,860, doi:10.1029/94JB00462.

Bradshaw, J. D. (1989), Cretaceous geotectonic patterns in the New Zealand region, *Tectonics*, *8*, 803–820, doi:10.1029/TC008i004p00803.

Bradshaw, J. D., R. J. Pankhurst, S. D. Weaver, B. C. Storey, R. J. Muir, and T. R. Ireland (1997), New Zealand superterranes recognized in Marie Byrd Land and Thurston Island, in *The Antarctic Region: Geological Evolution and Processes*, edited by C. A. Ricci, pp. 429–436, Terra Antarct. Publ., Siena, Italy.

Cande, S. C., C. A. Raymond, J. Stock, and W. F. Haxby (1995), Geophysics of the Pitman fracture zone, *Science*, *270*, 947–953, doi:10.1126/science.270.5238.947.

Chase, C. G. (1985), The geological significance of the geoid, *Annu. Rev. Earth Planet. Sci.*, *13*, 97–117, doi:10.1146/annurev.ea.13.050185.000525.

Chase, C. G., and D. R. Sprowl (1983), The modern geoid and ancient plate boundaries, *Earth Planet. Sci. Lett.*, *62*, 314–320, doi:10.1016/0012-821X(83)90002-X.

Cook, R. A., R. Sutherland, and H. Zhu (1999), *Cretaceous|Cenozoic geology and petroleum systems of the Great South Basin, New Zealand*, 188 pp., Inst. of Geol. and Nucl. Sci. Ltd., Lower Hutt, New Zealand.

Courtillot, V., A. Davaille, J. Besse, and J. Stock (2003), Three distinct types of hotspots in the Earth's mantle, *Earth Planet. Sci. Lett. 205*, 295–308, doi:10.1016/S0012-821X(02)01048-8.

Crough, S. T. (1983), The correction for sediment loading of the seafloor, *J. Geophys. Res.*, *88*, 6449–6454, doi:10.1029/JB088iB08p06449.

Cunningham, A. P., R. D. Larter, P. F. Barker, K. Gohl, and F. O. Nitsche (2002), Tectonic evolution of the Pacific margin of Antarctica 2. Structure of Late Cretaceous–early Tertiary plate boundaries in the Bellingshausen Sea from seismic reflection and gravity data, *J. Geophys. Res.*, *107*(B12), 2346, doi:10.1029/2002JB001897.

Dalziel, I. W. D., and D. H. Elliot (1982), West Antarctica: Problem child of Gondwanaland, *Tectonics*, *1*, 3–19, doi:10.1029/TC001i001p00003.

Davy, B., K. Hoernle, and R. Werner (2008), Hikurangi Plateau: Crustal structure, rifted formation, and Gondwana subduction history, *Geochem. Geophys. Geosyst.*, *9*, Q07004, doi:10.1029/2007GC001855.

Deschamps, F., and J. Trampert (2003), Mantle tomography and its relation to temperature and composition, *Phys. Earth Planet. Inter.*, *140*, 277–291, doi:10.1016/j.pepi.2003.09.004.

Ferris, J. K., A. P. M. Vaughan, and B. C. Storey (2000), Relics of a complex triple junction in the Weddell Sea embayment, Antarctica, *Earth Planet. Sci. Lett.*, *178*, 215–230, doi:10.1016/S0012-821X(00)00076-5.

Finn, C. A., R. D. Mueller, and K. S. Panter (2005), A Cenozoic diffuse alkaline magmatic province (DAMP) in the southwest Pacific without rift or plume origin, *Geochem. Geophys. Geosyst.*, *6*, Q02005, doi:10.1029/2004GC000723.

Flanagan, M. P., and P. M. Shearer (1998), Global mapping of topography on transition zone velocity discontinuities by stacking SS precursors, *J. Geophys. Res.*, *103*, 2673–2692, doi:10.1029/97JB03212.

Förste, C., et al. (2008), The GeoForschungsZentrum Potsdam/Groupe de Recherche de Geodesie Spatiale satellite-only and combined gravity field models: EIGEN-GL04S1 and EIGEN-GL04C, *J. Geod.*, *82*, 331–346, doi:10.1007/s00190-007-0183-8.

Forte, A. M., and J. X. Mitrovica (2001), Deep-mantle high-viscosity flow and thermochemical structure inferred from seismic and geodynamic data, *Nature*, *410*, 1049–1056, doi:10.1038/35074000.

Gaina, C., D. R. Müller, J.-Y. Royer, J. Stock, J. Hardebeck, and P. Symonds (1998), The tectonic history of the Tasman Sea: A puzzle with 13 pieces, *J. Geophys. Res.*, *103*, 12,413–12,433, doi:10.1029/98JB00386.

Grand, S. P. (2002), Mantle shear-wave tomography and the fate of subducted slabs, *Philos. Trans. R. Soc. Ser. A*, *360*, 2475–2491.

Gu, Y. J., A. M. Dziewonski, W. J. Su, and G. Ekstrom (2001), Models of the mantle shear velocity and discontinuities in the pattern of lateral heterogeneities, *J. Geophys. Res.*, *106*, 11,169–11,199, doi:10.1029/2001JB000340.

Gurnis, M., R. Müller, and L. Moresi (1998), Cretaceous vertical motion of Australia and the AustralianAntarctic discordance, *Science*, *279*, 1499–1504, doi:10.1126/science.279.5356.1499.

Gurnis, M., J. Mitrovica, J. Ritsema, and H. van Heijst (2000), Constraining mantle density structure using geological evidence of surface uplift rates: The case of the African superplume, *Geochem. Geophys. Geosyst.*, *1*, 1020, doi:10.1029/1999GC000035.

Hager, B. H. (1984), Subducted slabs and the geoid: Constraints on mantle rheology and flow, *J. Geophys. Res.*, *89*, 6003–6015, doi:10.1029/JB089iB07p06003.

Hager, B. H., R. W. Clayton, M. A. Richards, R. P. Comer, and A. M. Dziewonski (1985), Lower mantle heterogeneity, dynamic topography and the geoid, *Nature*, *313*, 541–546, doi:10.1038/313541a0.

Herve, F., R. J. Pankhurst, C. M. Fanning, M. Calderon, and G. M. Yaxley (2007), The South Patagonian batholith: 150 my of granite magmatism on a plate margin, *Lithos*, *97*, 373–394, doi:10.1016/j.lithos.2007.01.007.

Hirschmann, M. M. (2006), Water, melting, and the deep Earth H2O cycle, *Annu. Rev. Earth Planet. Sci.*, *34*, 629–653, doi:10.1146/annurev.earth.34.031405.125211.

Houser, C., G. Masters, M. Flanagan, and P. Shearer (2008), Determination and analysis of long-wavelength transition zone structure using SS precursors, *Geophys. J. Int.*, *174*, 178–194, doi:10.1111/j.1365-246X.2008.03719.x.

Karato, S., and B. B. Karki (2001), Origin of lateral variation of seismic wave velocities and density in the deep mantle, *J. Geophys. Res.*, *106*, 21,771–21,783, doi:10.1029/2001JB000214.

Kimbrough, D. L., A. J. Tulloch, D. S. Coombs, C. A. Landis, M. R. Johnston, and J. M. Mattinson (1994), Uranium-lead zircon ages from the Median Tectonic Zone, South Island, New Zealand, *N. Z. J. Geol. Geophys.*, *37*, 393–419.

King, P. R. (2000), Tectonic reconstructions of New Zealand 40 Ma to the present, *N. Z. J. Geol. Geophys.*, *43*, 611–638.

King, P. R., T. R. Naish, G. H. Browne, B. D. Field, and S. W. Edbrooke (1999), Cretaceous to Recent sedimentary patterns in New Zealand, *Folio Ser. 1*, GNS Sci., Inst. of Geol. and Nucl. Sci., Lower Hunt, N. Z.

King, S. D., and G. Masters (1992), An inversion for radial viscosity structure using seismic tomography, *Geophys. Res. Lett.*, *19*, 1551–1554, doi:10.1029/92GL01700.

Laird, M. G., and J. D. Bradshaw (2004), The break-up of a long-term relationship: The Cretaceous separation of New Zealand from Gondwana, *Gondwana Res.*, *7*, 273–286, doi:10.1016/S1342-937X(05)70325-7.

Larter, R. D., A. P. Cunningham, and P. F. Barker (2002), Tectonic evolution of the Pacific margin of Antarctica: 1. Late Cretaceous reconstructions, *J. Geophys. Res.*, *107*(B12), 2345, doi:10.1029/2000JB000052.

Lawver, L. A., J.-Y. Royer, D. T. Sandwell, and C. R. Scotese (1987), Evolution of the Antarctic continental margins, in *Geological Evolution of Antarctica*, edited by M. R. A. Thomson et al., pp. 533–539, Cambridge Univ. Press, Cambridge, U. K.

LeMasurier, W. E., and C. A. Landis (1996), Mantle-plume activity recorded by low-relief erosion surfaces in West Antarctica and New Zealand, *Geol. Soc. Am. Bull.*, *108*, 1450–1466, doi:10.1130/0016-7606(1996)108<1450:MPARBL>2.3.CO;2.

Liu, L., S. Spasojevic, and M. Gurnis (2008), Reconstructing Farallon Plate subduction beneath North America back to the Late Cretaceous, *Science*, *322*, 934–938, doi:10.1126/science.1162921.

Marks, K. M., and A. A. Tikku (2001), Cretaceous reconstructions of East Antarctica, Africa and Madagascar, *Earth Planet. Sci. Lett.*, *186*, 479–495, doi:10.1016/S0012-821X(01)00262-X.

Masters, G., G. Laske, H. Bolton, and A. Dziewonski (2000), The relative behavior of shear velocity, bulk sound speed, and compressional velocity in the mantle: Implications for chemical and thermal structure, in *Earth's Deep Interior: Mineral Physics and Tomography From the Atomic to the Global Scale*, *Geophys. Monogr. Ser.*, vol. 117, edited by S. Karato et al., pp. 63–88, AGU, Washington, D. C.

Mazengarb, C., and D. H. M. Harris (1994), Cretaceous stratigraphic and structural relationships of Raukumara Peninsula, New Zealand: Stratigraphic patterns associated with the migration of a thrust system, *Ann. Tecton.*, *8*, 100–118.

McCarron, J. J., and R. D. Larter (1998), Late Cretaceous to early Tertiary subduction history of the Antarctic Peninsula, *J. Geol. Soc.*, *155*, 255–268, doi:10.1144/gsjgs.155.2.0255.

Milne, G. A., J. X. Mitrovica, H. G. Scherneck, J. L. Davis, J. M. Johansson, H. Koivula, and M. Vermeer (2004), Continuous GPS measurements of postglacial adjustment in Fennoscandia: 2. Modeling results, *J. Geophys. Res.*, *109*, B02412, doi:10.1029/2003JB002619.

Mitrovica, J. X., and A. M. Forte (2004), A new inference of mantle viscosity based upon joint inversion of convection and glacial isostatic adjustment data, *Earth Planet. Sci. Lett.*, *225*, 177–189, doi:10.1016/j.epsl.2004.06.005.

Molnar, P., T. Atwater, J. Mammerickx, and S. M. Smith (1975), Magnetic anomalies, bathymetry and the tectonic evolution of the south Pacific since the Late Cretaceous, *Geophys. J. R. Astron. Soc.*, *40*, 383–420.

Mortimer, N., R. H. Herzer, P. B. Gans, D. L. Parkinson, and D. Seward (1998), Basement geology from Three Kings Ridge to West Norfolk Ridge, southwest Pacific Ocean: Evidence from petrology, geochemistry and isotopic dating of dredge samples, *Mar. Geol.*, *148*, 135–162, doi:10.1016/S0025-3227(98)00007-3.

Mortimer, N., A. J. Tulloch, R. N. Spark, N. W. Walker, E. Ladley, A. Allibone, and D. L. Kimbrough (1999), Overview of the Median Batholith, New Zealand: A new interpretation of the geology of the Median Tectonic Zone and adjacent rocks, *J. Afr. Earth Sci.*, *29*, 257–268, doi:10.1016/S0899-5362(99)00095-0.

Muir, R. J., S. D. Weaver, J. D. Bradshaw, G. N. Eby, and J. A. Evans (1995), The Cretaceous Separation Point Batholith, New Zealand: Granitoid magmas formed by melting of mafic lithosphere, *J. Geol. Soc.*, *152*, 689–701, doi:10.1144/gsjgs.152.4.0689.

Muir, R. J., T. R. Ireland, S. D. Weaver, J. D. Bradshaw, J. A. Evans, G. N. Eby, and D. Shelley (1998), Geochronology and geochemistry of a Mesozoic magmatic arc system, Fiordland, New Zealand, *J. Geol. Soc.*, *155*, 1037–1052, doi:10.1144/gsjgs.155.6.1037.

Mukasa, S. B., and I. W. D. Dalziel (2000), Marie Byrd Land, West Antarctica: Evolution of Gondwana's Pacific margin constrained by zircon

U-Pb geochronology and feldspar common-Pb isotopic compositions, *Geol. Soc. Am. Bull.*, *112*, 611–627, doi:10.1130/0016-7606(2000)112<611:MBLWAE>2.0.CO;2.

Müller, R. D., C. Gaina, A. Tikku, D. Mihut, S. C. Cande, and J. M. Stock (2000), Mesozoic/Cenozoic tectonic events around Australia, in *The History and Dynamics of Global Plate Motions*, *Geophys. Monogr. Ser.*, vol. 121, edited by M. A. Richards et al., pp. 161–188, AGU, Washington, D. C.

Nürnberg, D., and R. D. Müller (1991), The tectonic evolution of the South Atlantic from Late Jurassic to present, *Tectonophysics*, *191*, 27–53, doi:10.1016/0040-1951(91)90231-G.

Ohtani, E., M. Toma, T. Kubo, T. Kondo, and T. Kikegawa (2003), In situ X-ray observation of decomposition of superhydrous phase B at high pressure and temperature, *Geophys. Res. Lett.*, *30*(2), 1029, doi:10.1029/2002GL015549.

Ohtani, E., K. Litasov, T. Hosoya, T. Kubo, and T. Kondo (2004), Water transport into the deep mantle and formation of a hydrous transition zone, *Earth Planet. Sci. Lett.*, *143–144*, 255–269.

Pankhurst, R. J., T. R. Riley, C. M. Fanning, and S. P. Kelley (2000), Episodic silicic volcanism in Patagonia and the Antarctic Peninsula: Chronology of magmatism associated with the break-up of Gondwana, *J. Petrol.*, *41*, 605–625, doi:10.1093/petrology/41.5.605.

Paris, J.-P. (1981), Geology of New Caledonia: A synthetic text, *Mem. BRGM*, *113*, 1–278.

Richards, M. A., and B. H. Hager (1984), Geoid anomalies in a dynamic Earth, *J. Geophys. Res.*, *89*, 5987–6002, doi:10.1029/JB089iB07p05987.

Richards, M. A., B. H. Hager, and N. H. Sleep (1988), Dynamically supported geoid highs over hotspots: Observation and theory, *J. Geophys. Res.*, *93*, 7690–7708, doi:10.1029/JB093iB07p07690.

Ritsema, J., and H. J. van Heijst (2000), Seismic imaging of structural heterogeneity in Earth's mantle: Evidence for large-scale mantle flow, *Science Prog.*, *83*, 243–259.

Ritzwoller, M. H., N. M. Shapiro, A. L. Levshin, and G. M. Leahy (2001), Crustal and upper mantle structure beneath Antarctica and surrounding oceans, *J. Geophys. Res.*, *106*, 30,645–30,670, doi:10.1029/2001JB000179.

Rocchi, S., P. Armienti, M. D'Orazio, S. Tonarini, J. R. Wijbrans, and G. Di Vincenzo (2002), Cenozoic magmatism in the western Ross Embayment: Role of mantle plume versus plate dynamics in the development of the West Antarctic Rift System, *J. Geophys. Res.*, *107*(B9), 2195, doi:10.1029/2001JB000515.

Schellart, W. P., B. L. N. Kennett, W. Spakman, and M. Amaru (2009), Plate reconstructions and tomography reveal a fossil lower mantle slab below the Tasman Sea, *Earth Planet. Sci. Lett.*, *278*, 143–151, doi:10.1016/j.epsl.2008.11.004.

Sieminski, A., E. Debayle, and J. J. Leveque (2003), Seismic evidence for deep low-velocity anomalies in the transition zone beneath West Antarctica, *Earth Planet. Sci. Lett.*, *216*, 645–661, doi:10.1016/S0012-821X(03)00518-1.

Spasojevic, S., L. Liu, and M. Gurnis (2009), Adjoint models of mantle convection with seismic, plate motion and stratigraphic constraints: North America since the Late Cretaceous, *Geochem. Geophys. Geosyst.*, *10*, Q05W02, doi:10.1029/2008GC002345.

Steinberger, B., and A. R. Calderwood (2006), Models of large-scale viscous flow in the Earth's mantle with constraints from mineral physics and surface observations, *Geophys. J. Int.*, *167*, 1461–1481, doi:10.1111/j.1365-246X.2006.03131.x.

Stock, J. M., and P. Molnar (1987), Revised history of early Tertiary plate motion in the southwest Pacific, *Nature*, *325*, 495–499, doi:10.1038/325495a0.

Storey, B. C. (1995), The role of mantle plumes in continental breakup—Case histories from Gondwanaland, *Nature*, *377*, 301–308, doi:10.1038/377301a0.

Storey, B. C., and P. A. R. Nell (1988), Role of strike-slip faulting in the tectonic evolution of the Antarctic Peninsula, *J. Geol. Soc.*, *145*, 333–337, doi:10.1144/gsjgs.145.2.0333.

Storey, B. C., P. T. Leat, S. D. Weaver, R. J. Pankhurst, J. D. Bradshaw, and S. Kelley (1999), Mantle plumes and Antarctica-New Zealand rifting: Evidence from mid-Cretaceous mafic dykes, *J. Geol. Soc.*, *156*, 659–671, doi:10.1144/gsjgs.156.4.0659.

Sutherland, R. (1995), The Australia-Pacific boundary and Cenozoic plate motions in the SW Pacific: Some constraints from Geosat data, *Tectonics*, *14*, 819–831, doi:10.1029/95TC00930.

Sutherland, R. (1999a), Basement geology and tectonic development of the greater New Zealand region: An interpretation from regional magnetic data, *Tectonophysics*, *308*, 341–362, doi:10.1016/S0040-1951(99)00108-0.

Sutherland, R. (1999b), Cenozoic bending of New Zealand basement terranes and Alpine Fault displacement: A brief review, *N. Z. J. Geol. Geophys.*, *42*(2), 295–301.

Sutherland, R., S. Spasojevic, and M. Gurnis (2010), Mantle upwelling after Gondwana subduction death may explain anomalous topography of West Antarctica and subsidence history of eastern New Zealand, *Geology*, *38*, 155–158.

Tan, E., E. Choi, P. Thoutireddy, M. Gurnis, and M. Aivazis (2006), GeoFramework: Coupling multiple models of mantle convection within a computational framework, *Geochem. Geophys. Geosyst.*, *7*, Q06001, doi:10.1029/2005GC001155.

Veevers, J. J. (2000), Synopsis of momentous events in Australia's billion year history, in *Billion-Year Earth History of Australia and Neighbours in Gondwanaland: North Ryde, N.S.W.*, edited by J. J. Veevers, pp. 344–348, Gemoc Press, Sydney.

Veevers, J. J., P. J. Conaghan, and C. M. Powell (1994), Eastern Australia, *Geol. Soc. Am. Mem.*, *184*, 11–171.

Waight, T. E., S. D. Weaver, and R. J. Muir (1998), Mid-Cretaceous granitic magmatism during the transition from subduction to extension in southern New Zealand: A chemical and tectonic synthesis, *Lithos*, *45*, 469–482, doi:10.1016/S0024-4937(98)00045-0.

Weaver, S. D., B. Storey, R. J. Pankhurst, S. B. Mukasa, V. J. Divenere, and J. D. Bradshaw (1994), Antarctica-New Zealand rifting and Marie Byrd Land lithospheric magmatism linked to ridge subduction and mantle plume activity, *Geology*, *22*, 811–814, doi:10.1130/0091-7613(1994)022<0811:ANZRAM>2.3.CO;2.

Weissel, J. K., D. E. Hayes, and E. M. Herron (1977), Plate tectonic synthesis: The displacements between Australia, New Zealand, and Antarctica since the late Cretaceous, *Mar. Geol.*, *25*, 231–277, doi:10.1016/0025-3227(77)90054-8.

Zhong, S. J., M. T. Zuber, L. Moresi, and M. Gurnis (2000), Role of temperature-dependent viscosity and surface plates in spherical shell models of mantle convection, *J. Geophys. Res.*, *105*, 11,063–11,082, doi:10.1029/2000JB900003.

M. Gurnis and S. Spasojevic, Seismological Laboratory, California Institute of Technology, 1200 E. California Blvd., MC 252-21, Pasadena, CA 91125, USA. (Sonja@gps.caltech.edu)

R. Sutherland, GNS Science, P.O. Box 30368, Lower Hutt 5040, New Zealand.